

Gaussian Splashing: Direct Volumetric Rendering Underwater

Nir Mualem
Ben-Gurion University
nirmu@post.bgu.ac.il

Roy Amoyal
Ben-Gurion University
amoyalr@post.bgu.ac.il

Oren Freifeld
Ben-Gurion University
orenfr@cs.bgu.ac.il

Derya Akkaynak
The Inter-University Institute for Marine Sciences and the University of Haifa
dakkaynak@univ.haifa.ac.il

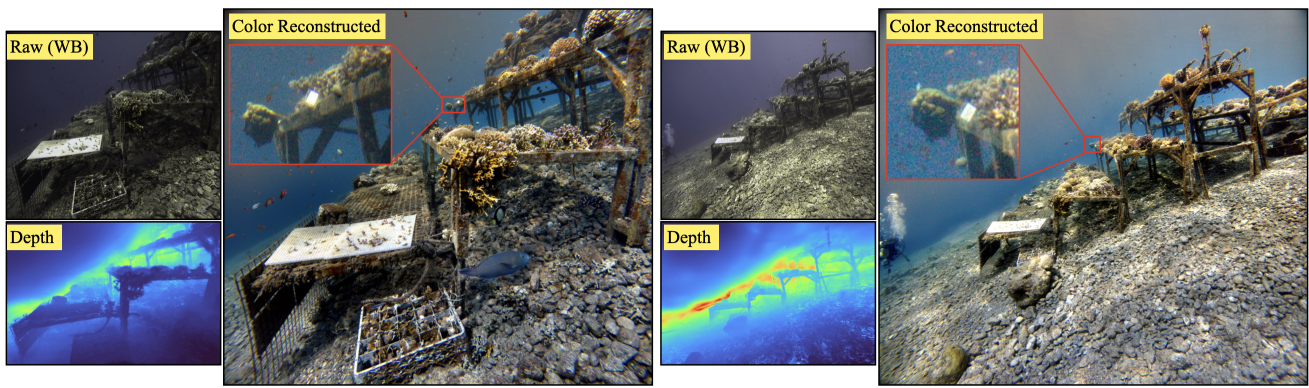


Figure 1. Gaussian Splashing can reconstruct accurate geometry for underwater scenes in minutes, and render novel views in real-time. Here, we demonstrate an application in color reconstruction: we used the depth maps produced by our method from raw (but white balanced - WB) images as inputs to the original Sea-thru algorithm [2], which requires an accurate depth map to estimate medium parameters. The results, shown here on images from two different distances from the *TableDB* dataset we contribute, show excellent visual quality, even for distant scene details.

Abstract

In underwater images, most useful features are occluded by water. The extent of the occlusion depends on imaging geometry and can vary even across a sequence of burst images.

As a result, 3D reconstruction methods robust on in-air scenes, like Neural Radiance Field methods (NeRFs) or 3D Gaussian Splatting (3DGS), fail on underwater scenes. While a recent underwater adaptation of NeRFs achieved state-of-the-art results, it is impractically slow: reconstruction takes hours and its rendering rate, in frames per second (FPS), is less than 1. Here, we present a new method that takes only a few minutes for reconstruction and renders novel underwater scenes at 140 FPS. Named Gaussian Splashing, our method unifies the strengths and speed of 3DGS with an image formation model for capturing scattering, introducing innovations in the rendering and depth estimation procedures and in the 3DGS loss function. Despite the com-

plexities of underwater adaptation, our method produces images at unparalleled speeds with superior details. Moreover, it reveals distant scene details with far greater clarity than other methods, dramatically improving reconstructed and rendered images. We demonstrate results on existing datasets and a new dataset we have collected.

1. Introduction

Understanding and interpreting underwater scenes pose unique challenges for computer vision. Image features that would be important for downstream tasks such as detection, segmentation, classification, and tracking, *etc.*, are commonly occluded by color distortions and haze, which arise due to the distance- and wavelength-dependent attenuation of light in the water. It may seem straightforward that, if we could consistently remove the degrading effects of water from underwater photographs, existing computer vision methods would be readily applicable. However, in practice, this is challenging.

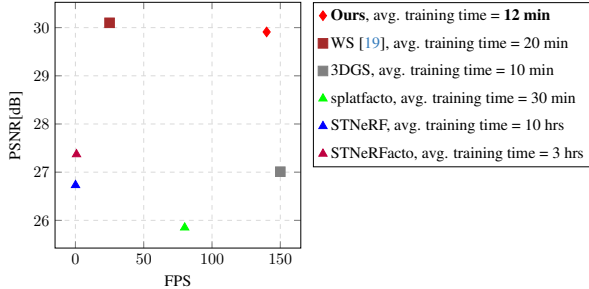


Figure 2. Comparison of methods by Frames Per Second (FPS) and Peak Signal-to-Noise Ratio (PSNR). Our approach (red diamonds) achieves an impressive PSNR average of 29.11 while maintaining high inference speeds for real-time rendering. The PSNR values were averaged over the Red Sea, Curaçao, Panama and TableDB datasets (the FPS rates are fairly consistent across datasets).

In the physical world, light attenuation in water is governed only by the constituents of the water body. In a photograph, the attenuation parameters have little relation to those of the real world scene; they are specific to the image, the imager, and the conditions under which the image was captured [1, 3]. Consequently, in wideband terms, there are no universal medium parameters representing a water ‘type’, or rules that can be generalized to all underwater images. Therefore, for successful color reconstruction—and, by extension, to perform downstream tasks like detection and segmentation—medium parameters must be estimated per image, alongside scene depth.

Recently, Akkaynak & Treibitz demonstrated with the Sea-thru algorithm [2] that if the scene depth is known, medium parameters can easily be estimated (Figure 1). Depth for underwater scenes is most commonly obtained from multiple images in pre-processing, *e.g.*, through Structure-From-Motion (SFM) [2, 34], or more recently, neural radiance fields (NeRFs) [18]. Unfortunately, however, it is not yet possible to obtain scene depth underwater, in real-time, without using multiple cameras or specialized sensors. Underwater-specific monocular depth estimation methods (*e.g.*, [4, 10, 37, 48, 49]) are performing increasingly better, but do not yet produce accurate enough results when scenes are turbid or objects are heavily occluded by backscatter, and do not generalize to scenes captured under different optical conditions. Depth Anything [44], while not trained exclusively for underwater, also fails in generalizing to underwater scenes even though it boasts excellent zero-shot depth estimation ability for a diverse set of land scenes. Thus, robust estimation of scene geometry from multiple images—but using as few images as possible—remains to be the most promising direction to pursue.

When it comes to recovering scene geometry from a sparse set of images, NeRFs have achieved immense success [9, 24]. While classic approaches for scene representa-

tion relied on explicit geometric models (*e.g.*, meshes [38]), neural rendering employs functions [26] or data structures ([8], [11]) to capture the scene’s appearance and geometry. In a fresh perspective in neural rendering, NeRFs learn an implicit function to represent the scene’s radiance at every point in space. Levy *et al.* [18] were the first to take NeRFs underwater, adapting the original rendering equation for image formation in a scattering medium. Their method, Seathru-NeRF, achieved state-of-the-art (SOTA) results for novel-view synthesis and color reconstruction for underwater scenes. However, while successful as a prototype algorithm, the practicality of Seathru-NeRF is limited by its performance—requiring 15-20 images and approximately 3 hours for training [33, 36]. Even on more powerful hardware and with more optimized implementations, it is difficult to achieve faster training and near real-time rendering as the requirement to evaluate the implicit function along viewing rays during rendering makes NeRF-based methods inherently computationally expensive.

Fortunately, a recent (non-neural) radiance field method, 3D Gaussian Splatting (3DGS) [13], emerges as an alternative that, we argue, is intrinsically more suitable for adaptation to underwater scenes. Briefly,

3DGS represents the scene via a finite set of anisotropic 3D Gaussians, augmented with opacity and color information. Importantly,

the algorithm from [13] achieves accelerated training (\sim mins) and lends itself to real-time novel view synthesis. As with most computer-vision methods, however, 3DGS does not readily work on underwater scenes. To fill this gap, we proposed a new method, called *Gaussian Splashing*, which is an adaptation of 3DGS specific to underwater scenes, and yet its speed is on par with 3DGS. *The key insight behind the proposed approach is that the entire underwater image formation formulation can be integrated seamlessly into the 3DGS data representation and the 3DGS rendering pipeline. Consequently, we were able to implement our new algorithm, by its entirety, in CUDA, without having to resort to external (i.e., non-CUDA) computations. In turn, this facilitates a smoother backpropagation process and lets the method achieve state-of-the-art performance with minimal rendering time, establishing it as the fastest in this domain.*

Our main contributions are:

- 1. New method:** The novelty of the method is fourfold. 1) At its core Gaussian Splashing uses a new rendering equation based on the Sea-thru image formation model [2] for scattering media. 2) The new rendering equation alters the original loss function (from [13]) by making it also dependent on learnable backscatter coefficients and depth. 3) We also add a new loss term related to those coefficients. 4) We propose a new depth estimation procedure and combine it within the overall optimization.
- 2. SOTA results:** for geometry estimation (especially for far away pixels under

high backscatter), scene color reconstruction, and reconstruction of high-frequency areas (*i.e.*, sharp visual detail); see, *e.g.*, Figure 1. **3. Speed:** Fast training (\sim mins) and real-time rendering (see, *e.g.*, Figure 2) despite the fact that we work with the images in their original high resolution (*i.e.*, no down-sampling as is mandated by the NeRF-based methods), and real-time novel-view synthesis of original and color-reconstructed scenes. This speed is obtained by the virtue of both our algorithm design and the fact that the entire algorithm is implemented in pure CUDA (with a user-friendly python wrapper).

4. New dataset: We collected a dataset of images of an underwater 3D scene. Unlike existing such datasets, ours presents a large variability in terms of camera-to-scene distances.

Our results and the speed of our method are a significant step forward towards overcoming the primary bottleneck—robust depth estimation—that has prevented underwater computer vision from achieving the progress and performance in-air computer vision has enjoyed in the last decade.

2. Related Work

Given the different and more complex image formation process underwater, we focus here on works in the underwater realm. For the in-land case, recent reviews of NeRF-based methods and 3DGS methods can be found in [46] and [7], respectively.

Due to the logistical difficulties and costs of collecting high-quality, calibrated data at sea, there are markedly fewer studies on scene reconstruction and novel-view synthesis underwater than for scenes on land.

NeRF-based methods. `WaterNeRF` [32] uses an atmospheric image formation model and histogram-equalized images to estimate medium parameters. `WaterHE-NeRF` [50] utilizes the Retinex theory for attenuation removal, which is meant to compensate for spatially-varying illumination. That method is limited to close-range scenes where backscatter is small. `Seathru-NeRF` [18] was the first NeRF using an image formation model for scattering. While it achieved SOTA results on novel-view synthesis and color reconstruction, both its training and inference were very slow. Moreover, that method has difficulties with accurately capturing scene details that are far from the camera (that said, in that aspect other existing methods do even worse as capturing such details underwater is hard). Lian *et al.* [21] proposed a framework to quantify the uncertainty in underwater scenes rendered via NeRFs, but did not propose a new way to render. Additionally, it focused only on scenes illuminated with white light (*i.e.*, deep sea imagery), which makes it inapplicable to the outputs of all other methods using physics-based image formation models, such as `Seathru-NeRF`.

3DGS [13], central to our paper, offers a different approach to scene representation by explicitly modeling scenes

with 3D Gaussians, augmented with color and opacity information. Unlike NeRFs, which rely on implicit representations, 3DGS offers both enhanced interpretability and intuitive manipulation of scene geometry. Its rendering method, utilizing splatting (*i.e.*, projecting 3D Gaussians to 2D), analytic derivatives, and a tile-based processing, enables rapid estimation of the parameters of the augmented Gaussians. Importantly, by replacing the complex processes of NeRF with a discrete representation and direct rendering, 3DGS achieves real-time rendering during inference, marking a significant improvement in rendering efficiency and performance. To our knowledge, **thus far only one peer-reviewed published work applied 3DGS to underwater scenes:** Qu *et al.* devised `Z-Splat` [27], a 3DGS extension that incorporates sonar data to address the “missing cone problem”. That method, however, requires not only optical data but also acoustical data (hence requires specialized instrumentation), in contrast to our pure vision-based multi-view approach.

During the writing of this paper, we became aware of three recent ArXiv papers that describe works that were conducted concurrently to ours. These works, like ours, aim at adapting 3DGS to underwater scenes. However, those works combine 3DGS with neural nets [19] [39], a fact negatively impacting their rendering time, or introduce extra learnable parameters and numerous loss terms to achieve model fit [43]. As of the time of the writing of our paper, only one of these three, `WaterSplatting` [19], has published code so far, so we could not directly compare results. A future comprehensive comparison between all of the four concurrent works (theirs and ours) will be interesting. In any case, note that our method, which unlike those methods 1) does not require deep nets and 2) is implemented purely in CUDA, is *much* faster than those works. In terms of performance, our method achieves comparable results to [19] (the best performing method among those works). See, *e.g.*, Figure 2.

3. Preliminaries

3.1. 3D Gaussian Splatting (3DGS)

3DGS [13] represents a 3D scene by N 3D Gaussians, each of which is augmented with two more attributes: color and opacity. Let $\theta_i = (\boldsymbol{\mu}_i, \mathbf{m}\Sigma_i, \mathbf{c}_i, \sigma_i)$ denote the parameters of Gaussian i , where $\boldsymbol{\mu}_i \in \mathbb{R}^3$ is its 3D position (*i.e.*, its mean), $\mathbf{m}\Sigma_i$, a 3-by-3 symmetric positive-definite matrix, is its covariance matrix, $\mathbf{c}_i \in \mathbb{R}^3$ is the color (represented by Spherical Harmonics), and $\sigma_i \geq 0$ is the opacity. Thus, $\Theta \triangleq (\theta_i)_{i=1}^N$ represents the entire scene.

If Θ and the camera pose are known, the corresponding 2D image can be generated by rendering the scene. The rendering process accumulates the contributions from each Gaussian (based on differentiable point-based rendering techniques [16] [42] [40]) along viewing rays to generate the

image as follows. Given the camera pose, the 2D location of a pixel defines a ray, in 3D, from the camera origin to the pixel. Let $\mathbf{p}_i \in \mathbb{R}^3$ be the closest point, among all of the points on the ray, to $\boldsymbol{\mu}_i$. The pixel’s color, denoted by \mathbf{C} , is computed using a technique called α -compositing:

$$\mathbf{C} = \sum_{i=1}^M \mathbf{c}_i \alpha_i T_i, \quad T_i \triangleq \prod_{j=0}^{i-1} (1 - \alpha_j), \quad (1)$$

where $M < N$, and, in a slight abuse of notation, possibly renaming indices, the M Gaussians participating in Eq. 1 are sorted in an increasing order according to their depth (*i.e.*, the distance from the camera), and $\alpha_i > 0$ is the opacity contribution of Gaussian i to this pixel, defined by

$$\alpha_i = \text{sigmoid}(\sigma_i) e^{-\frac{1}{2}(\mathbf{p}_i - \boldsymbol{\mu}_i)^T \mathbf{m} \Sigma_i^{-1} (\mathbf{p}_i - \boldsymbol{\mu}_i)}. \quad (2)$$

Typically, the pixel-dependent number $M \ll N$; *i.e.*, only a small subset of the N Gaussians affects the pixel’s color. How the subset is chosen will be clear later when we discuss tiles. Also, in practice, $(\mathbf{p}_i - \boldsymbol{\mu}_i)^T \mathbf{m} \Sigma_i^{-1} (\mathbf{p}_i - \boldsymbol{\mu}_i)$ is computed in 2D (not 3D) using an affine projection that approximates the camera’s projection of \mathbf{p}_i , $\boldsymbol{\mu}_i$, and $\mathbf{m} \Sigma_i$; see [51] for details. Note that $\alpha_i \in [0, 1] \forall i$, and that the effect of T_i , which is called the *transmittance* of Gaussian i (for that particular pixel), is that the first $i - 1$ Gaussians (whose depths are smaller than that of Gaussian i) down weight the color contribution of Gaussian i according to their opacity, covariance matrices, and distances from the ray.

To achieve real-time rendering, 3DGS employs two strategies [5]: **1) Tiles:** To avoid computing contribution of every Gaussian for every pixel, the image is divided into non-overlapping patches, called *tiles*, of 16×16 pixels. Among the N 2D projected Gaussians, only those close enough (*e.g.*, less than several standard deviations) to the tile are deemed relevant for that tile (the other Gaussians are ignored). Thus, during the rendering of a pixel, the α -compositing (Eq. 2) uses only the projected Gaussians associated with the tile containing the pixel. In other words, all the pixels within the a tile share the value of M . **2) Parallel Rendering:** The tile-based approach, together with the direct rendering, facilitates massive parallelism that leads to huge speedups.

So far we discussed the forward problem; *i.e.*, how a 2D image is rendered given Θ and the camera pose. The inverse problem, which uses the forward one as a sub-routine, is as follows: given a collection of 2D images and the associated estimated camera poses, reconstruct the 3D scene by optimizing over Θ . This reconstruction is also referred to as the *learning* of the scene. After the reconstruction, novel view synthesis (*i.e.*, *generalization*) is done by rendering the scene given a new camera pose.

Finally, compositing techniques are often employed during post-processing of 3DGS to combine the contributions from various effects (*e.g.*, lighting, materials, anti-aliasing [12], [22], [45]).

3.2. Underwater Image Formation

By definition, clear air does not attenuate light so image formation models for clear air do not include the medium parameters. When the medium is attenuating (*e.g.*, atmospheric haze, fog, smog, and all water bodies), an image formation model must include, at a minimum, two processes that affect light: out-scattering from the scene as light travels towards the camera (commonly referred to as *attenuation*, which causes color distortions), and in-scattering from the water volume between the camera and the scene (*i.e.*, commonly referred to as *backscatter* or path radiance, which causes haze/visibility loss). We adapt the Sea-thru image formation model [1] that includes both these processes and is applicable to scenes that are either in air or underwater:

$$I = \underbrace{J}_{\text{clean image}} \cdot \underbrace{(e^{-\beta_d(\mathbf{v}_d) \cdot z})}_{\text{attenuation}} + \underbrace{B^\infty}_{\text{color at } \infty} \cdot \underbrace{(1 - e^{-\beta_b(\mathbf{v}_b) \cdot z})}_{\text{backscatter}}. \quad (3)$$

Here, I is the image captured by the camera and has attenuated colors while J is the clean image “without water”. The terms β_d and β_b are wideband medium parameters governing attenuation and backscatter, respectively, and they have dependencies \mathbf{v}_d and \mathbf{v}_b on object reflectance, spectrum of ambient light, spectral response of the camera, and physical attenuation coefficients of the water body, all of which are wavelength-dependent functions. B^∞ is the saturated color of water at infinity, *i.e.*, the signal present in areas without objects, and z is the scene depth, which must be known for each pixel. The *direct signal* governs how the colors of the objects in the scene are affected by the distance that the light travels in a given water body, and the *backscatter signal* governs the density and color of the “fog” occluding the scene. The backscatter signal exists due to the scattering in the water volume and is independent of the scene/objects.

It is important to note that the camera sensor is assumed to have a linear response to light, otherwise Eq. 3 does not hold. Similarly, the image from which the parameters will be estimated must also be linear, meaning in-camera processed .jpg images or gamma-corrected images cannot be used, unless the non-linearities can be reversed.

4. The Proposed Method: Gaussian Splashing

Unsurprisingly, as we will show in § 6, in underwater scenes 3DGS is very limited. Hence, we extend the traditional 3DGS by introducing three additional learnable parameters and adapt the rendering procedure to accommodate scattering (§ 4.1). Similarly, we modify depth estimation for underwater conditions (§ 4.2), thereby altering the original loss terms used in 3DGS, and introduce an additional related loss term (§ 4.3). In § 4.4 we discuss our pure-CUDA implementation. Figure 3 depicts the entire method.

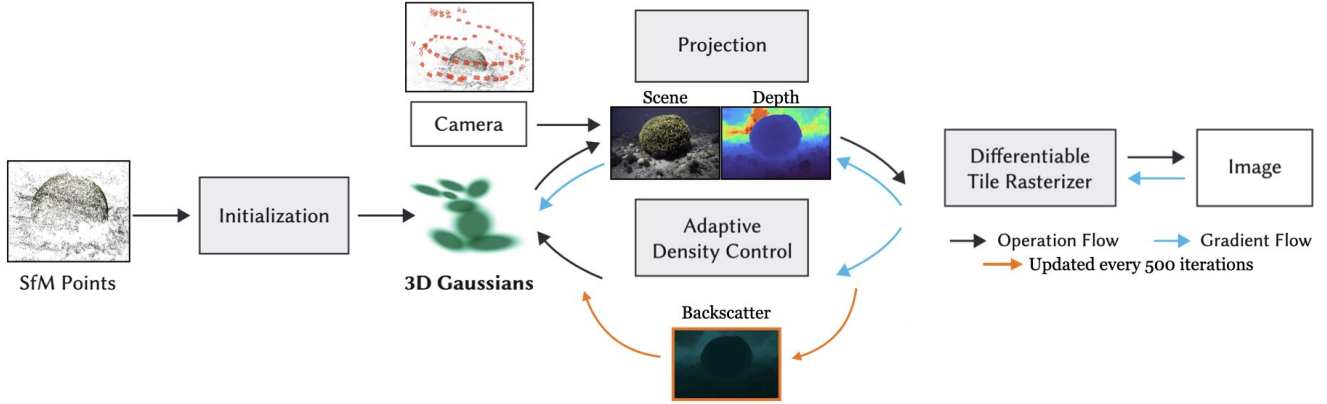


Figure 3. Method overview: Initially, we utilize Structure from Motion (SfM) to acquire an initial point cloud and camera poses. Subsequently, we commence the optimization process to refine the model based on our underwater rendering equation and modified tile rasterization, taking those distortions into account. We evaluate backscatterer every 500 steps to ensure convergence towards the accurate medium coefficients using our approach. The base figure is adapted from the original 3D Gaussian Splatting method in [13].

4.1. Direct Rendering for Underwater Scenes

According to [1], $\beta_b(\mathbf{v}_d)$ can be treated as constant within an image, while β_d mainly varies with the object distance (*i.e.*, z) and to a lesser extent with object reflectance. Similarly, all dependencies of $\beta_d(\mathbf{v}_d)$ can be assumed to be small [3], except for that on the scene depth z , which we model to be linear. Thus, Eq. 4 is well approximated by

$$I = \underbrace{J}_{\text{clean image}} \cdot \underbrace{(e^{-B_d \cdot z})}_{\text{attenuation}} + \underbrace{B_\infty}_{\text{color at } \infty} \cdot \underbrace{(1 - e^{-B_b \cdot z})}_{\text{backscatter}} \quad (4)$$

where B_b is a constant approximating $\beta_b(\mathbf{v}_d)$ and B_d is a constant such that $B_d \cdot z \approx \beta_d(\mathbf{v}_d) \cdot z$ (*i.e.*, the linear dependency of $\beta_d(\mathbf{v}_d)$ on z is absorbed into B_d)

Analogously to [18], who extended NeRF to underwater scenes, we incorporate backscatter and attenuation effects into the 3DGS formulation. Utilizing the coefficients from Eq. 4, we propose a new rendering formula for *Gaussian Splashing* (namely, Gaussian Splatting underwater):

$$C_{\text{uw}} = \left(\sum_{i=1}^M c_i \alpha_i T_i \right) e^{-B_d z} + B_\infty (1 - e^{-B_b z}) \quad (5)$$

where $T_i \triangleq \prod_{j=0}^{i-1} (1 - \alpha_j)$. Here, C_{uw} is the final color for the underwater scene, while B_d is the direct attenuation parameter and the pair (B_∞, B_b) are the backscatter attenuation parameters. We emphasize that B_d , B_∞ , and B_b are *learnable* parameters and are not assumed to be known beforehand. The other variables in Eq. 5 are as in Eq. 1.

4.2. Estimating Dense Depth Maps

When using 3DGS for land scenes, there is usually no need to estimate dense depth maps. However, in the underwa-

ter case, color distortions strongly depend on scene depth (among other factors). Drawing inspiration from methodologies in [23] and [6], we propose a technique for extracting the depth z from (based on a current estimate of Θ) while leveraging the rasterization pipeline (further details in § 4.3). Concretely, upon the rendering of an image, at each pixel we extract the depth, denoted by z , as

$$z = \left(\sum_{i=1}^M d_i \alpha_i T_i \right) / \left(\sum_{i=1}^M \alpha_i T_i \right) \quad (6)$$

where d_i is the depth of Gaussian i . As we will explain in § 4.3, during the optimization we use Eq. 6 to extract the z values and these help in guiding the learning.

4.3. Optimization

The original loss function used in [13] is relatively simple, comprising two widely-used losses,

$$\sum_{k=1}^K (1 - \lambda_1) \|I_k^{\text{gt}} - I_k^r(\Theta)\|_{\ell_1} + \lambda_1 \mathcal{L}_{\text{D-SSIM}}(I_k^{\text{gt}}, I_k^r(\Theta)), \quad (7)$$

where K is the number of images, $\lambda_1 \in [0, 1]$ is user-defined, I_k^{gt} and I_k^r are i -th ground truth (*i.e.*, observed) image and i -th rendered image, respectively, $\|\cdot\|_{\ell_1}$ is the ℓ_1 norm, and $\mathcal{L}_{\text{D-SSIM}}$ [41] measures the structural similarity between the two images, providing a perceptually-motivated metric.

Let $B_s = B_\infty (1 - e^{-B_b \cdot z})$ denote the true-but-unknown backscatter (from Eq. 4) at a pixel. One of the advantages of 3DGS over NeRF-based methods is the ability to quickly render entire images during the optimization process. This is in sharp contrast to NeRFs which, due to computational reasons, must render only a small number (*e.g.*, 500) of randomly-chosen pixels during the optimization [24] [26] [20]. The fast rendering lets us, during the

optimization, obtain rough estimates of B_∞ and B_b from the rendered images. To better estimate the backscattering parameters, we introduce an additional loss, denoted by \mathcal{L}_{bs} , inspired by the backscatter-estimation method outlined in [2]. Backscatter increases with depth z and eventually saturates [1, 2]. Thus, shadowed areas across the entire image provide a good estimate of the backscatter without the direct signal. Initially, we divide the depth map obtained from the current estimate of the scene (see § 4.2) into 10 evenly-spaced clusters covering the range from the minimal value of z to the maximal. Within each cluster, we identify, in the ground-truth image, the pixels whose RGB triplets are below the bottom 1st percentile. These triplets serve as an overestimate of the backscatter, which we model as

$$\widehat{B}_s = \widehat{B}_\infty(1 - e^{-\widehat{B}_b z}) \quad (8)$$

where \widehat{B}_s and z are the color value and depth estimate at such a pixel. Given the pairs of (\widehat{B}_s, z) values, we use nonlinear least squares fitting to estimate parameters \widehat{B}_∞ and \widehat{B}_b for each RGB channel while ensuring they remain within the bounds $[0, 1]$ and $[0, 5]$, respectively. The full algorithm for estimating these parameters appears in the Appendix.

While those estimates, \widehat{B}_∞ and \widehat{B}_b , are fairly effective, rather than using them directly, we opt to learn the parameters as part of the overall optimization, during which we let those estimates merely guide the learning of the B_∞ and B_b parameters. Concretely, our proposed loss function is

$$\begin{aligned} \mathcal{L}(\Theta, B_d, B_\infty, B_b) = & \\ & \sum_{k=1}^K (1 - \lambda_1) \|I_k^{\text{gt}} - I_k^r(\Theta, B_d, B_\infty, B_b)\|_{\ell_1} + \\ & \lambda_1 \mathcal{L}_{\text{D-SSIM}}(I_k^{\text{gt}}, I_k^r(\Theta, B_d, B_\infty, B_b)) + \lambda_2 \mathcal{L}_{bs}(B_\infty, B_b) \end{aligned} \quad (9)$$

where $\lambda_2 > 0$ is user defined and $\mathcal{L}_{bs}(B_\infty, B_b) = \|B_\infty - \widehat{B}_\infty\|_{\ell_1} + \|B_b - \widehat{B}_b\|_{\ell_1}$. As the depth maps improve during the optimization process, every 500 iterations we re-compute (using Eq. 6 and the nonlinear least squares procedure mentioned earlier) the \widehat{B}_∞ and \widehat{B}_b quantities that appear in \mathcal{L}_{bs} . This approach represents an alternate learning strategy, where the iterative improvement of depth maps leads to the refinement of \widehat{B}_∞ and \widehat{B}_b , which we then utilize for improving the optimization over the 3D scene (which, in turn, impacts the depth, z ; see Eq. 6). Therefore, the additional loss term facilitates better reconstruction and depth estimation in underwater scenes.

It is important to note that the difference between Eq. 7 and Eq. 9 is not just (the periodic inclusion of) \mathcal{L}_{bs} but also the fact that in Eq. 9, the rendered images (which appear in the $\|\cdot\|_{\ell_1}$ and $\mathcal{L}_{\text{D-SSIM}}$ loss terms in both equations) are functions of Θ, B_d, B_∞ , and B_b (not just Θ).

To minimize Eq. 9 over Θ, B_d, B_∞ , and B_b we employ the Adam optimizer [15], utilizing the same learning rate as

in [13]. Our additional parameters (*i.e.*, B_d, B_∞ , and B_b) are trained using the same learning rate as each Gaussian color parameter c_i . The details of the partial derivatives for all our additional parameters appear in the Appendix.

To recap, our approach is grounded in an established formulation of underwater image formation that we use to adapt the 3DGS rendering to aquatic environments. Together with our proposed additional loss term and gradual depth estimation, this lets us propose a fast and effective method for underwater 3D reconstruction and novel view synthesis.

4.4. Implementation

We incorporate the extraction of the depth map z from the 3DGS representation using our own customized CUDA implementation. Empirically, the best result was achieved by mapping our depth to $[0, 1.0]$ by the (shifted and scaled) logistic function, $z = 2/(1 + e^{-0.1 \cdot \widehat{z}}) - 1$ where \widehat{z} is the initial output of 3DGS manipulation based on [6]. This logistic function transforms the original depth values to ensure they fall within the desired range for underwater visualization.

Leveraging the insights from [13], we have developed a CUDA-based package that harnesses the power of the differential rasterization pipeline. This approach ensures both speed and efficiency in integrating our extra parameters tailored to underwater scenes.

Finally, in [14], one of the steps in 3DGS, the so-called densification process (addition and removal of Gaussians), was recently improved by using an MCMC approach to sample Gaussians for subsequent iterations. We adopt this improvement, as we found it beneficial for capturing high-frequency details in the scene.

5. New Dataset

Noting that existing public underwater datasets are limited in terms of the variation in camera-to-scene distances, we captured a new underwater dataset (TableDB). It consists of 172 images with a resolution of 1384×918 pixels (see our Appendix for example images), and, unlike existing public datasets, it is unbounded in terms camera-to-scene distances. That dataset will be made available upon acceptance.

6. Experiments and Results

Datasets and Camera Pose Extraction. In addition to our TableDB we also experimented on several publicly available underwater datasets from [18]. We used COLMAP [30, 31] to extract camera poses and utilized its sparse 3D point initialization to determine the initial positions of the Gaussians.

Competing methods and evaluation metrics. The key work that has performed 3D reconstruction and rendering for underwater scenes in natural environments is Sea-Thru NeRF (STNeRF) [18], which serves as the primary comparison in terms of quality. There are two implementations of STNeRF:

Table 1. Quantitative Comparison.

Dataset	Red Sea			Curaçao			Panama			TableDB		
Method	PSNR \uparrow	SSIM \uparrow	LPIPS \downarrow	PSNR \uparrow	SSIM \uparrow	LPIPS \downarrow	PSNR \uparrow	SSIM \uparrow	LPIPS \downarrow	PSNR \uparrow	SSIM \uparrow	LPIPS \downarrow
3DGS [13]	22.94	0.87	0.17	28.23	0.88	0.23	29.88	0.91	0.15	31.17	0.91	0.12
splatfacto [22]	21.65	0.85	0.20	25.30	0.88	0.19	30.61	0.93	0.07	32.51	0.92	0.06
STNeRF [18]	21.83	0.77	0.25	30.48	0.87	0.20	27.89	0.83	0.22	29.76	0.86	0.15
STNeRFacto [33]	23.17	0.86	0.14	28.42	0.89	0.12	30.53	0.92	0.07	18.7	0.63	0.42
Gaussian Splashing (Ours)	24.73	0.92	0.11	31.26	0.92	0.17	31.35	0.94	0.11	32.33	0.95	0.09

one using [25] as the NeRF backbone package, and another by [35], where Nerfacto, a powerful NeRF version, is used as the backbone. We refer to the latter as STNeRFacto. We compare our work to both implementations. Recall that our approach improves upon the original 3DGS [13] in that it adapts it to aquatic scenes by incorporating the related ocean optics. Therefore, we also performed comparisons to [13] and Splatfacto by [47], as the latter achieves the best results for in-the-wild scenes. We measure performance using three widely-used metrics: PSNR, LPIPS, and SSIM. Peak Signal-to-Noise Ratio (PSNR) quantifies image quality by measuring the ratio between the maximal possible power of a signal and the power of the corrupting noise. Learned Perceptual Image Patch Similarity (LPIPS) assesses perceptual similarity by comparing deep features extracted from neural networks, as in [17], providing a human-aligned evaluation of visual similarity. Structural Similarity Index (SSIM) evaluates image similarity based on luminance, contrast, and structure, thereby capturing perceptual differences that align closely with human visual perception.

Hyper-parameters, memory and computational resources. In our experiments, we set $\lambda_2 = 0.1$ and $\lambda_1 = 0.3$. All of the other hyper-parameters values are as in [13]; see our appendix for details. Training was conducted on a single NVIDIA GeForce RTX 4090 GPU. The average memory consumption per scene over 30,000 training steps was approximately 500 MB, which is slightly less than STNeRF’s average of around 600 MB.

6.1. Results

Figure 4 shows a visual comparison between the methods. A quantitative analysis, summarized in Table 1, shows the effectiveness of the proposed method. Being based on 3DGS, our method is very fast, much faster than the NeRF-based methods. For example, its training takes only several minutes and, during inference, it renders images at 140 frames per second (FPS) on average (across different datasets). Please see the appendix for a comprehensive comparison between the different methods in terms of running times during both training and inference. Table 1 also shows that vanilla 3DGS (while being fast) struggles to effectively handle underwater scenes (see also Figure 4). This is in sharp contrast with our method which offers both speed and quality.

Although traditional metrics like PSNR might be mis-

leading in underwater scenarios due to the predominant bluish color palette, our method’s superiority becomes evident upon closer inspection, particularly when examining distant objects within the scene. This advantage is particularly pronounced with datasets like TableDB, which unlike publicly-available datasets, is unbounded in viewpoints and scene depth. Of note, our method stands out in preserving the original resolution of rendered scenes due to its efficient rendering speed, as shown in Figure 2. In contrast, STNeRF and STNeRFacto must downsize the images during training. For additional visual results, see the appendix. Also, for best impression, we strongly encourage the reader to see our videos in [our project webpage](#).

6.2. Ablation Study

Our ablation study, summarized in Table 2, considered several conditions: 1) Removing our additional loss term \mathcal{L}_{bs} ; 2) Forcing B_d to be zero, to test if B_s alone can capture enough of the underwater scene distortions. 3) Using original densification process from [13] instead of MCMC densification process approach [14]. 4) Replacing our depth estimation with a standard monocular depth model ([28] [29]). For completeness, Table 2 also includes, as a baseline, the original 3DGS [13], as well as our complete model. As Table 2 shows, all of the components turn out to be important.

7. Conclusion

We presented *Gaussian Splashing*, a variant of 3D-Gaussian Splatting specialized for underwater imagery. Our method accurately estimates geometry for underwater scenes, from as few as five images, which is a necessary step to maximize the amount of useful information that can be extracted from the original images containing attenuated colors. Perhaps more importantly, our method performs geometry estimation from a handful of scenes within a few minutes (compared to several hours for NeRF-based methods)

We are unaware of any potential negative societal impact of this work. Having accurate scene geometry is a necessary component for consistent color reconstruction, following which underwater imagery can be processed using powerful computer-vision and machine-learning methods developed for in-air images. Thus, getting close to near real-time training opens the possibility for real-time color reconstruction

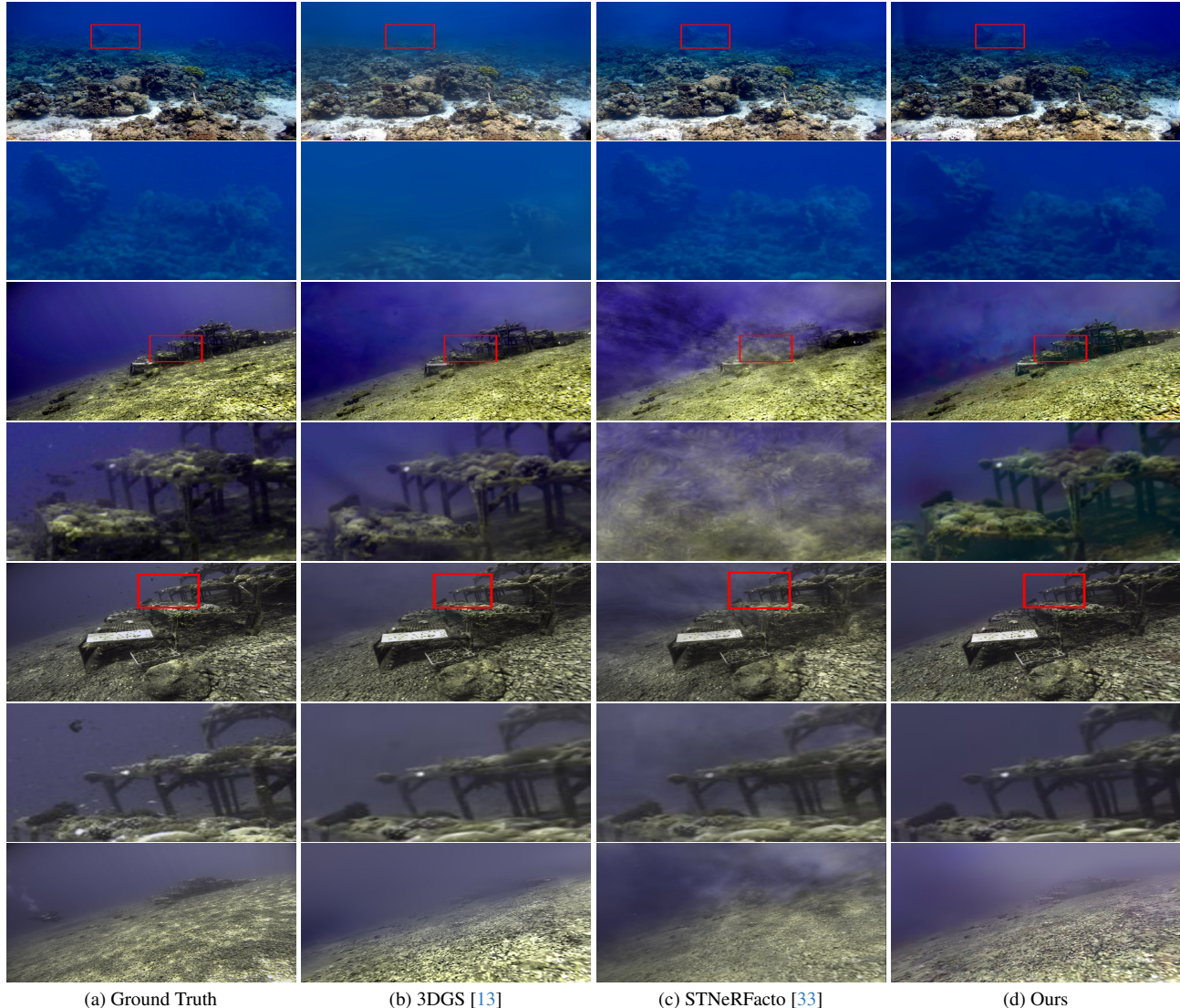


Figure 4. Visual Comparison of novel views. Row 1: an example from the Red-Sea scene. Row 3/5/7: examples from the TableDB dataset. Rows 2/4/6: zoom in on the red rectangles in Rows 1/3/5. Note that Row 7 highlights STNeRFacto’s failure on unbounded scenes.

Table 2. Ablation Study

Dataset	Red Sea			Curaçao			Panama			Avg.		
	PSNR \uparrow	SSIM \uparrow	LPIPS \downarrow	PSNR \uparrow	SSIM \uparrow	LPIPS \downarrow	PSNR \uparrow	SSIM \uparrow	LPIPS \downarrow	PSNR \uparrow	SSIM \uparrow	LPIPS \downarrow
3DGS [13] (the baseline)	22.94	0.87	0.17	28.23	0.88	0.23	29.88	0.91	0.15	27.02	0.89	0.18
Ours w/o \mathcal{L}_{bs}	22.93	0.88	0.14	20.65	0.79	0.27	27.67	0.87	0.21	23.75	0.85	0.20
Ours w/o B_d	22.12	0.88	0.15	30.12	0.89	0.20	29.47	0.91	0.13	27.24	0.89	0.16
Ours w/o MCMC densification	23.04	0.88	0.15	28.40	0.89	0.23	29.99	0.91	0.14	27.14	0.89	0.31
Ours w/o depth	21.16	0.84	0.23	23.86	0.80	0.24	27.69	0.88	0.21	24.23	0.84	0.23
Our complete method	24.73	0.92	0.11	31.26	0.92	0.17	31.35	0.94	0.11	29.11	0.92	0.13

of underwater scenes, which would improve capabilities of autonomous or remotely operated underwater vehicles for better navigation, SLAM, and obstacle avoidance. Lastly, leveraging well-estimated scene geometry, we are able to render novel-views of underwater scenes in real time. This

capability can have a broad and positive societal impact as it immediately enables applications for subsea training (*e.g.*, divers or submarine pilots, search and rescue teams, commercial divers, *etc.*), computer games, marine science education, and cultural heritage documentation. Our method shares

three limitations with [18, 33]:

1) While, like [18, 33], we rely on a SOTA image formation model, that model does not address phenomena such as multiple scattering or artificial illumination. 2) The method requires the extraction of camera poses, which is hard if the visibility is too poor (as in, *e.g.*, turbid water). This limitation is shared with not only [18, 33] but also other NeRF-based or 3DGS-based methods. 3) While our formulation’s strength lies in its ability to learn the medium’s characteristics, the success of that learning depends on having enough variation in scene range. However, while [18, 33] struggle if the inter-image range variability is *too large* (see Figure 4), our method handles such cases gracefully.

Acknowledgment

This project was partially funded by the US Office of Naval Research (US ONR).

References

- [1] Derya Akkaynak and Tali Treibitz. A revised underwater image formation model. In *CVPR*, 2018. 2, 4, 5, 6
- [2] Derya Akkaynak and Tali Treibitz. Sea-thru: A method for removing water from underwater images. In *CVPR*, 2019. 1, 2, 6, 12
- [3] Derya Akkaynak, Tali Treibitz, Tom Shlesinger, Roni Tamir, Yossi Loya, and David Iluz. What is the space of attenuation coefficients in underwater computer vision? In *CVPR*, 2017. 2, 5
- [4] Shlomi Amitai, Itzik Klein, and Tali Treibitz. Self-supervised monocular depth underwater. In *IEEE ICRA*, 2023. 2
- [5] Guikun Chen and Wenguan Wang. A survey on 3d Gaussian splatting, 2024. 4
- [6] Jaeyoung Chung, Jeongtaek Oh, and Kyoung Mu Lee. Depth-regularized optimization for 3d Gaussian splatting in few-shot images. *ArXiv*, 2023. 5, 6
- [7] Ben Fei, Jingyi Xu, Rui Zhang, Qingyuan Zhou, Weidong Yang, and Ying He. 3d Gaussian as a new vision era: A survey. *arXiv preprint arXiv:2402.07181*, 2024. 3
- [8] Sara Fridovich-Keil, Alex Yu, Matthew Tancik, Qinhong Chen, Benjamin Recht, and Angjoo Kanazawa. Plenoxels: Radiance fields without neural networks. In *CVPR*, 2022. 2
- [9] Kyle Gao, Yina Gao, Hongjie He, Dening Lu, Linlin Xu, and Jonathan Li. Nerf: Neural radiance field in 3d vision, a comprehensive review. *arXiv preprint arXiv:2210.00379*, 2022. 2
- [10] Honey Gupta and Kaushik Mitra. Unsupervised single image underwater depth estimation. In *ICIP*. IEEE, 2019. 2
- [11] Szymon Jabłoński and Tomasz Martyn. Real-time voxel rendering algorithm based on screen space billboard voxel buffer with sparse lookup textures, 2016. 2
- [12] Yingwenqi Jiang, Jiadong Tu, Yuan Liu, Xifeng Gao, Xiaoxiao Long, Wenping Wang, and Yuexin Ma. Gaussianshader: 3d Gaussian splatting with shading functions for reflective surfaces. *arXiv preprint arXiv:2311.17977*, 2023. 4
- [13] Bernhard Kerbl, Georgios Kopanas, Thomas Leimkühler, and George Drettakis. 3d Gaussian splatting for real-time radiance field rendering. *ACM Transactions on Graphics*, 2023. 2, 3, 5, 6, 7, 8, 16, 20
- [14] Shakiba Kheradmand, Daniel Rebain, Gopal Sharma, Weiwei Sun, Jeff Tseng, Hossam Isack, Abhishek Kar, Andrea Tagliasacchi, and Kwang Moo Yi. 3d gaussian splatting as markov chain monte carlo. *arXiv preprint arXiv:2404.09591*, 2024. 6, 7
- [15] Diederik P. Kingma and Jimmy Ba. Adam: A method for stochastic optimization. *CoRR*, 2014. 6
- [16] Georgios Kopanas, Julien Philip, Thomas Leimkühler, and George Drettakis. Point-based neural rendering with per-view optimization. *Computer Graphics Forum (Proceedings of the Eurographics Symposium on Rendering)*, 2021. 3
- [17] Alex Krizhevsky, Ilya Sutskever, and Geoffrey E. Hinton. ImageNet classification with deep convolutional neural networks. *Communications of the ACM*, 2012. 7
- [18] Deborah Levy, Amit Peleg, Naama Pearl, Dan Rosenbaum, Derya Akkaynak, Simon Korman, and Tali Treibitz. Seathru-nerf: Neural radiance fields in scattering media. In *CVPR*, 2023. 2, 3, 5, 6, 7, 9, 16, 20
- [19] Huapeng Li, Wenxuan Song, Tianao Xu, Alexandre Elsig, and Jonas Kulhanek. WaterSplatting: Fast underwater 3D scene reconstruction using gaussian splatting. *arXiv*, 2024. 2, 3
- [20] Zhaoshuo Li, Thomas Müller, Alex Evans, Russell H Taylor, Mathias Unberath, Ming-Yu Liu, and Chen-Hsuan Lin. Neuralangelo: High-fidelity neural surface reconstruction. In *CVPR*, 2023. 5
- [21] Haojie Lian, Xinhao Li, Leilei Chen, Xin Wen, Mengxi Zhang, Jieyuan Zhang, and Yilin Qu. Uncertainty quantification of neural reflectance fields for underwater scenes. *Journal of Marine Science and Engineering*, 2024. 3
- [22] Zhihao Liang, Qi Zhang, Wenbo Hu, Ying Feng, Lei Zhu, and Kui Jia. Analytic-splatting: Anti-aliased 3d Gaussian splatting via analytic integration, 2024. 4, 7, 16
- [23] Jonathon Luiten, Georgios Kopanas, Bastian Leibe, and Deva Ramanan. Dynamic 3d Gaussians: Tracking by persistent dynamic view synthesis. *ArXiv*, 2023. 5
- [24] Ben Mildenhall, Pratul P. Srinivasan, Matthew Tancik, Jonathan T. Barron, Ravi Ramamoorthi, and Ren Ng. Nerf: Representing scenes as neural radiance fields for view synthesis. In *ECCV*, 2020. 2, 5
- [25] Ben Mildenhall, Dor Verbin, Pratul P. Srinivasan, Peter Hedman, Ricardo Martin-Brualla, and Jonathan T. Barron. Multi-NeRF: A Code Release for Mip-NeRF 360, Ref-NeRF, and RawNeRF, 2022. 7
- [26] Thomas Müller, Alex Evans, Christoph Schied, and Alexander Keller. Instant neural graphics primitives with a multiresolution hash encoding. *ACM ToG*, 2022. 2, 5
- [27] Ziyuan Qu, Omkar Vengurlekar, Mohamad Qadri, Kevin Zhang, Michael Kaess, Christopher Metzler, Suren Jayasuriya, and Adithya Kumar Pediredla. Z-splat: Z-axis Gaussian splatting for camera-sonar fusion. *ArXiv*, 2024. 3
- [28] René Ranftl, Katrin Lasinger, David Hafner, Konrad Schindler, and Vladlen Koltun. Towards robust monocular depth estimation: Mixing datasets for zero-shot cross-dataset transfer. *IEEE TPAMI*, 2020. 7
- [29] René Ranftl, Alexey Bochkovskiy, and Vladlen Koltun. Vision transformers for dense prediction. *ArXiv preprint*, 2021. 7
- [30] Johannes Lutz Schönberger and Jan-Michael Frahm. Structure-from-motion revisited. In *CVPR*, 2016. 6
- [31] Johannes Lutz Schönberger, Enliang Zheng, Marc Pollefeys, and Jan-Michael Frahm. Pixelwise view selection for unstructured multi-view stereo. In *ECCV*, 2016. 6
- [32] Advait Venkatraman Sethuraman, Manikandasriram Srinivasan Ramanagopal, and Katherine A Skinner. Waternerf: Neural radiance fields for underwater scenes. In *OCEANS 2023-MTS/IEEE US Gulf Coast*, 2023. 3
- [33] Paul Setinek. Seathru-nerf: Nerf studio. https://github.com/AkerBP/seathru_nerf, 2023. 2, 7, 8, 9, 16
- [34] Mengkun She, Felix Seegräber, David Nakath, and Kevin Köser. Refractive colmap: Refractive structure-from-motion revisited. *arXiv preprint arXiv:2403.08640*, 2024. 2

- [35] Matthew Tancik, Ethan Weber, Evonne Ng, Ruilong Li, Brent Yi, Justin Kerr, Terrance Wang, Alexander Kristoffersen, Jake Austin, Kamyar Salahi, Abhik Ahuja, David McAllister, and Angjoo Kanazawa. Nerfstudio: A modular framework for neural radiance field development. *SIGGRAPH*, 2023. 7
- [36] Matthew Tancik, Ethan Weber, Evonne Ng, Ruilong Li, Brent Yi, Justin Kerr, Terrance Wang, Alexander Kristoffersen, Jake Austin, Kamyar Salahi, Abhik Ahuja, David McAllister, and Angjoo Kanazawa. Nerfstudio: A modular framework for neural radiance field development. In *SIGGRAPH*, 2023. 2
- [37] Nisha Varghese, Ashish Kumar, and AN Rajagopalan. Self-supervised monocular underwater depth recovery, image restoration, and a real-sea video dataset. In *ICCV*, 2023. 2
- [38] Vishal Verma and Ekta Walia. 3d rendering - techniques and challenges. *International Journal of Engineering and Technology*, 2010. 2
- [39] Haoran Wang, Nantheera Anantrasirichai, Fan Zhang, and David Bull. Uw-gs: Distractor-aware 3d gaussian splatting for enhanced underwater scene reconstruction. *ArXiv*, 2024. 3
- [40] Yifan Wang, Felice Serena, Shihao Wu, Cengiz Öztireli, and Olga Sorkine-Hornung. Differentiable surface splatting for point-based geometry processing. *ACM TOG*, 2019. 3
- [41] Zhou Wang, Eero P. Simoncelli, and Alan Conrad Bovik. Multiscale structural similarity for image quality assessment. In *Asilomar Conference on Signals, Systems & Computers*, 2003. 5
- [42] Olivia Wiles, Georgia Gkioxari, Richard Szeliski, and Justin Johnson. Synsin: End-to-end view synthesis from a single image. In *CVPR*, 2019. 3
- [43] Daniel Yang, John J. Leonard, and Yogesh Girdhar. Seasplat: Representing underwater scenes with 3d gaussian splatting and a physically grounded image formation model. *arxiv*, 2024. 3
- [44] Lihe Yang, Bingyi Kang, Zilong Huang, Xiaogang Xu, Jiashi Feng, and Hengshuang Zhao. Depth anything: Unleashing the power of large-scale unlabeled data. In *CVPR*, 2024. 2
- [45] Zeyu Yang, Hongye Yang, Zijie Pan, and Li Zhang. Real-time photorealistic dynamic scene representation and rendering with 4d Gaussian splatting. In *ICLR*, 2024. 4
- [46] Mingyuan Yao, Yukang Huo, Yang Ran, Qingbin Tian, Ruifeng Wang, and Haihua Wang. Neural radiance field-based visual rendering: A comprehensive review. *arXiv preprint arXiv:2404.00714*, 2024. 3
- [47] Vickie Ye and Angjoo Kanazawa. Mathematical supplement for the gsplat library. *ArXiv*, 2023. 7
- [48] Boxiao Yu, Jiayi Wu, and Md Jahidul Islam. Udepth: Fast monocular depth estimation for visually-guided underwater robots. In *IEEE ICRA*, 2023. 2
- [49] Fan Zhang, Shaodi You, Yu Li, and Ying Fu. Atlantis: Enabling underwater depth estimation with stable diffusion. In *Proceedings of the IEEE/CVF Conference on Computer Vision and Pattern Recognition*, pages 11852–11861, 2024. 2
- [50] Jingchun Zhou, Tianyu Liang, Zongxin He, Dehuan Zhang, Weishi Zhang, Xianping Fu, and Chongyi Li. Waterhe-nerf: Water-ray tracing neural radiance fields for underwater scene reconstruction. *arXiv preprint arXiv:2312.06946*, 2023. 3
- [51] Matthias Zwicker, Hanspeter Pfister, Jeroen van Baar, and Markus H. Gross. Ewa splatting. *IEEE Trans. Vis. Comput. Graph.*, 2002. 4

A. Supplemental Material

A.1. Additional Visual Results

Qualitative videos showcasing comparisons, depth estimation, and backscattering estimation, including videos for frames from our new TableDB dataset, are available on [our project webpage](#), and we strongly encourage viewing them to get a better impression and deeper understanding. Additional rendering results for training images and novel views are presented in [Figure 6](#) and [Figure 7](#), where [Figure 7](#) includes several images from our new TableDB dataset (more examples from TableDB are available in our anonymous webpage). [Figure 8](#) provides visualizations of depth estimation. Furthermore, [Figure 5](#) illustrates another example of color reconstruction that can be efficiently achieved using our fast method.

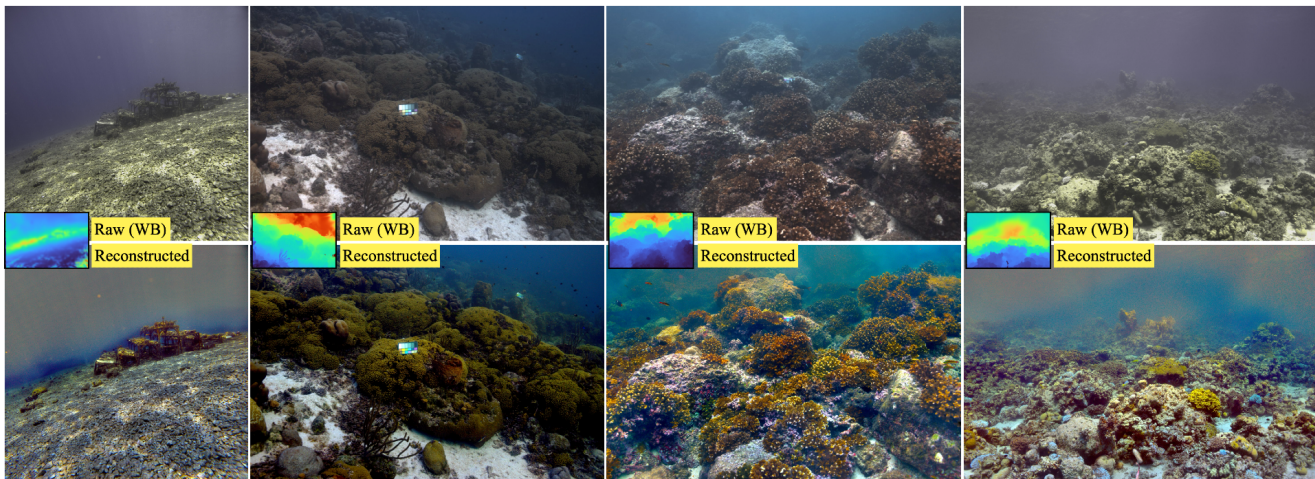
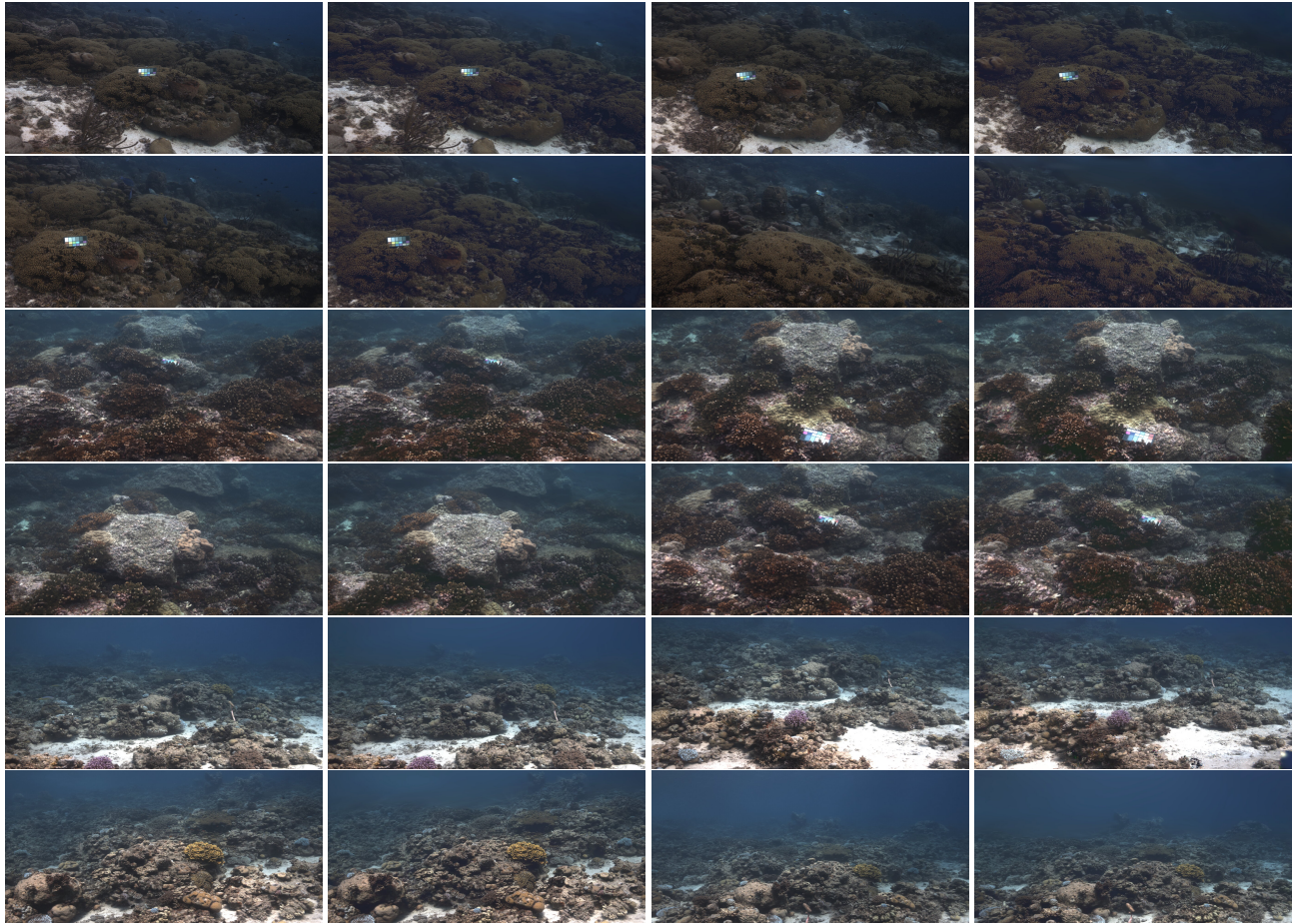


Figure 5. Color reconstruction application utilizing depth maps generated by our method, with raw (white-balanced, WB) images as inputs to the original Sea-thru algorithm [2]. Results are presented across all datasets.



(a) Ground Truth (train)

(b) Rendered (train)

(c) Ground Truth (test)

(d) Rendered (test)

Figure 6. Supplementary rendering results exemplifying the effectiveness and visual quality of our method across three different scenes and conditions. Train refers to the data used during the reconstruction. Test refers to novel views.

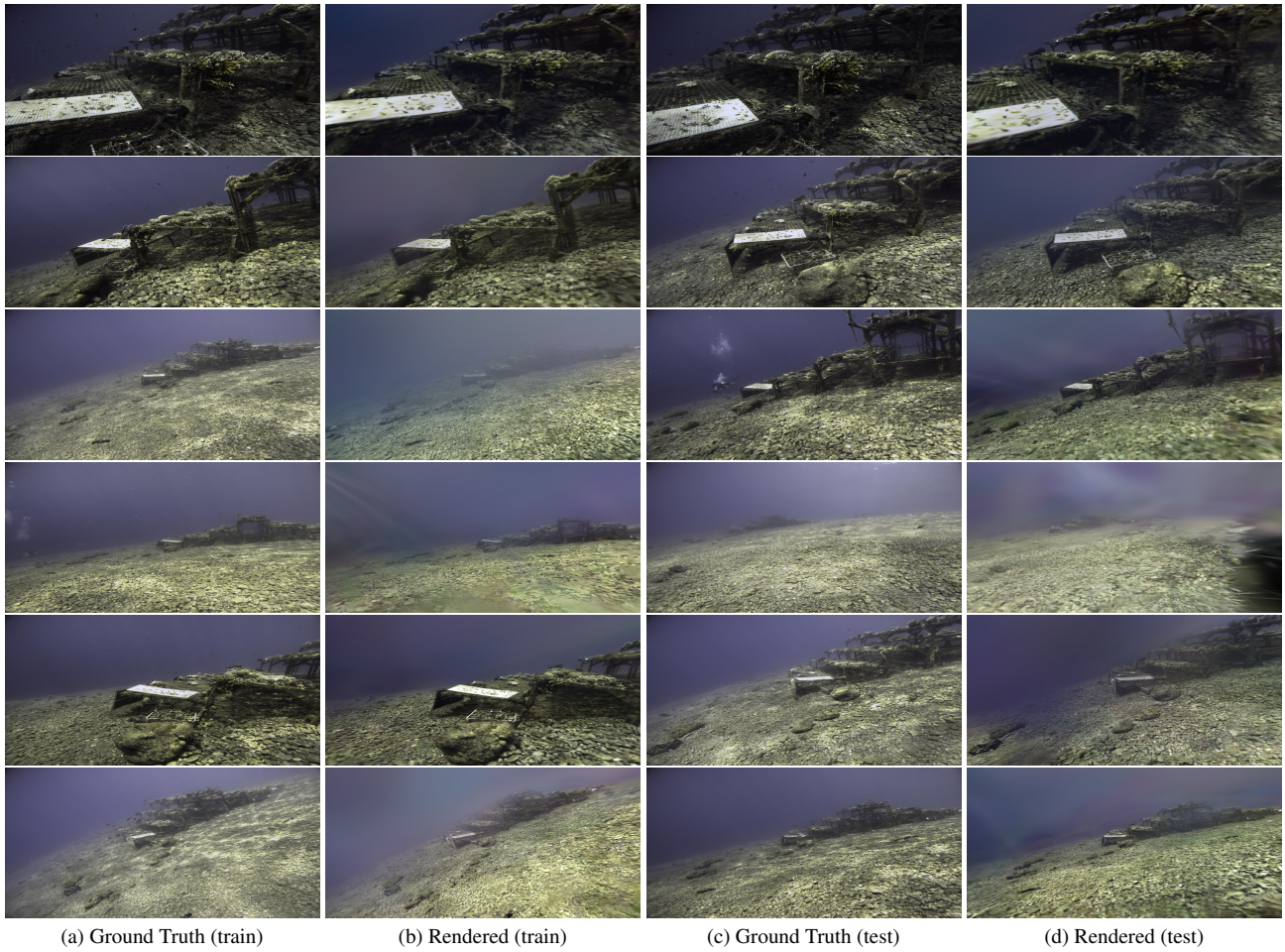


Figure 7. Supplementary rendering results demonstrating the effectiveness and visual quality of our method on the TableDB dataset. TableDB is a distinctive underwater dataset featuring a wide range of depths. "Train" refers to data used for reconstruction, while "Test" represents novel views.

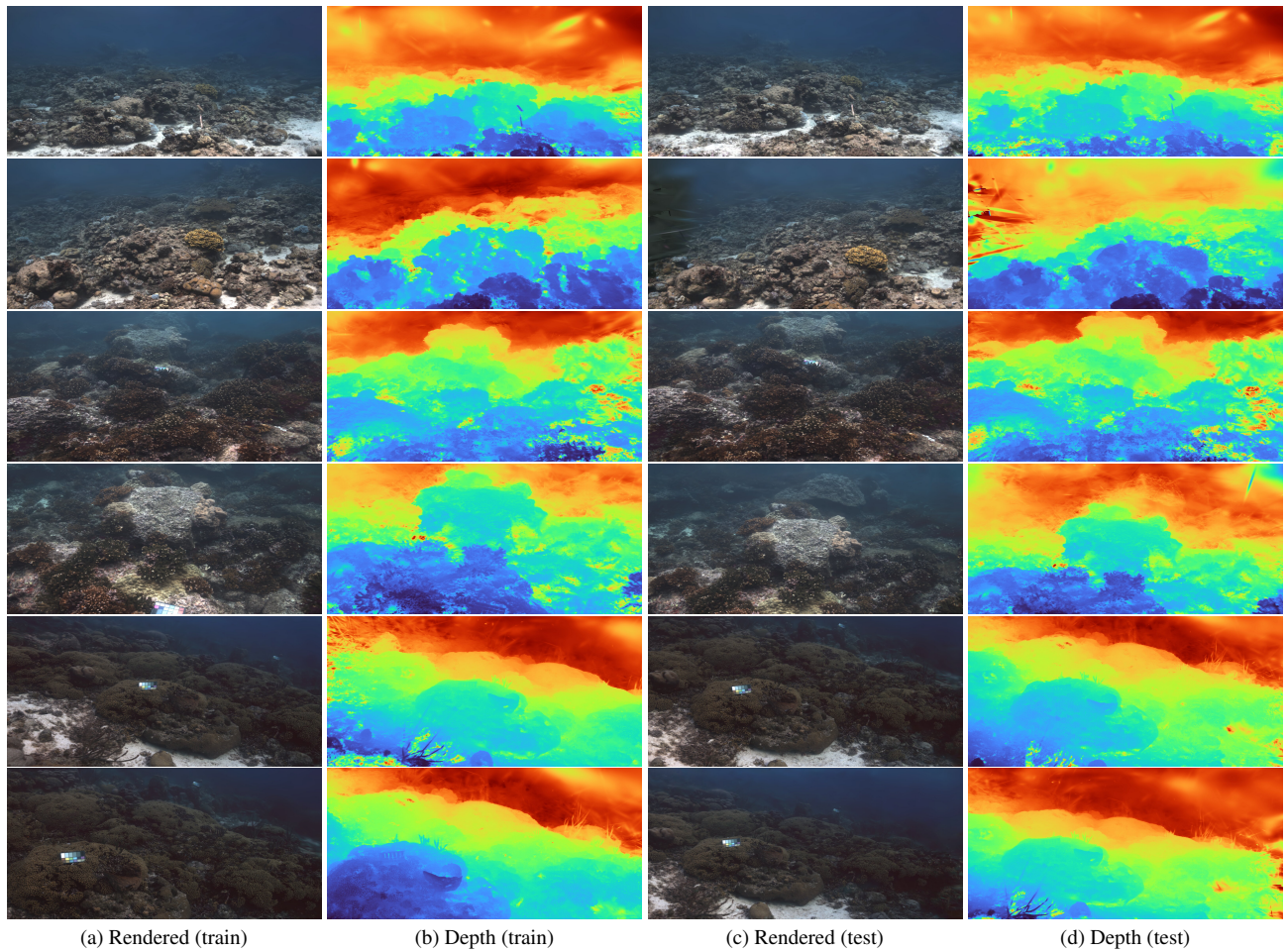


Figure 8. Rendered views and novel views, along with the depth maps generated by our method, shown for scenes from the Red Sea, Panama, and Curaçao.

A.2. Time Comparison

Measuring the rendering time of our method reveals that it is significantly faster than competitors in both training and inference. The high frame rate achieved during rendering enables its use in real-time applications while maintaining accuracy at such speeds. Detailed results are summarized in [Table 3](#).

Dataset	Red Sea		Curaçao		TableDB	
	FPS↑	Training Time (min)↓	FPS↑	Training Time (min)↓	FPS↑	Training Time (min)↓
3DGS [13]	174	10	154	13	162	16
splatfacto [22]	129	28	111	25	119	37
STNeRF [18]	0.05	582	0.05	547	0.06	612
STNeRfacto [33]	0.72	168	0.76	151	0.53	213
Gaussian Splashing (Ours)	187	11	135	12	161	15

Table 3. Comprehensive comparison table across scenes, highlighting the frames per second (FPS) performance during rendering and the training time (minutes) required to create the model.

A.3. Partial Derivatives of the New Parameters

$$\begin{aligned}
C_{\text{UW}} &= \left[\sum_{i=1}^N \mathbf{c}_i \alpha_i \cdot T_i \right] e^{-B_d z} + B_\infty (1 - e^{-B_b z}) \\
&= \left[\sum_{i=1}^N \mathbf{c}_i \alpha_i \cdot \prod_{j=0}^{i-1} (1 - \alpha_j) \right] e^{-B_d z} + B_\infty (1 - e^{-B_b z})
\end{aligned} \tag{10}$$

$$\begin{aligned}
\frac{\partial \mathcal{L}}{\partial \mathbf{c}_i} &= \frac{\partial C_{\text{UW}}}{\partial \mathbf{c}_i} \cdot e^{-B_d z} \cdot \frac{\partial \mathcal{L}}{\partial C_{\text{UW}}} \\
&= \alpha_i T_i \cdot e^{-B_d z} \cdot \frac{\partial \mathcal{L}}{\partial C_{\text{UW}}} \\
&= \alpha_i \prod_{j=0}^{i-1} (1 - \alpha_j) \cdot e^{-B_d z} \cdot \frac{\partial \mathcal{L}}{\partial C_{\text{UW}}}
\end{aligned} \tag{11}$$

$$\begin{aligned}
\frac{\partial \mathcal{L}}{\partial \alpha_i} &= \frac{\partial C_{\text{UW}}}{\partial \alpha_i} \cdot e^{-B_d z} \cdot \frac{\partial \mathcal{L}}{\partial C_{\text{UW}}} \\
&= \left[\mathbf{c}_i \cdot T_i - \sum_{j=i+1}^{N-1} \mathbf{c}_j \alpha_j \frac{T_j}{(1 - \alpha_i)} \right] \cdot e^{-B_d z} \cdot \frac{\partial \mathcal{L}}{\partial C_{\text{UW}}} \\
&= \left[\mathbf{c}_i \prod_{j=0}^{i-1} (1 - \alpha_j) - \sum_{j=i+1}^{N-1} \mathbf{c}_j \alpha_j \left(\prod_{k=0}^{i-1} (1 - \alpha_k) \prod_{k=i+1}^{j-1} (1 - \alpha_k) \right) \right] \cdot e^{-B_d z} \cdot \frac{\partial \mathcal{L}}{\partial C_{\text{UW}}}
\end{aligned} \tag{12}$$

$$\begin{aligned}
\frac{\partial \mathcal{L}}{\partial B_d} &= - \sum_{i=1}^N (\mathbf{c}_i \alpha_i T_i) \cdot e^{-B_d z} \cdot \frac{\partial \mathcal{L}}{\partial C_{\text{UW}}} \\
&= - \sum_{i=1}^N \left(\mathbf{c}_i \alpha_i \prod_{j=0}^{i-1} (1 - \alpha_j) \right) \cdot e^{-B_d z} \cdot \frac{\partial \mathcal{L}}{\partial C_{\text{UW}}}
\end{aligned} \tag{13}$$

$$\frac{\partial \mathcal{L}}{\partial B_b} = \left(\frac{\partial \mathcal{L}}{\partial C_{\text{UW}}} \right) B_\infty e^{-B_b z} + \lambda_2 \tag{14}$$

$$\frac{\partial \mathcal{L}}{\partial B_\infty} = \left(\frac{\partial \mathcal{L}}{\partial C_{\text{UW}}} \right) (1 - e^{-B_b z}) + \lambda_2 \tag{15}$$

A.4. Backscatter Estimation

The backscatter estimation algorithm is outlined in [Algorithm 1](#), which calls [Algorithm 2](#) as a subroutine. A visual explanation of underwater attenuation is provided in [Figure 9](#).

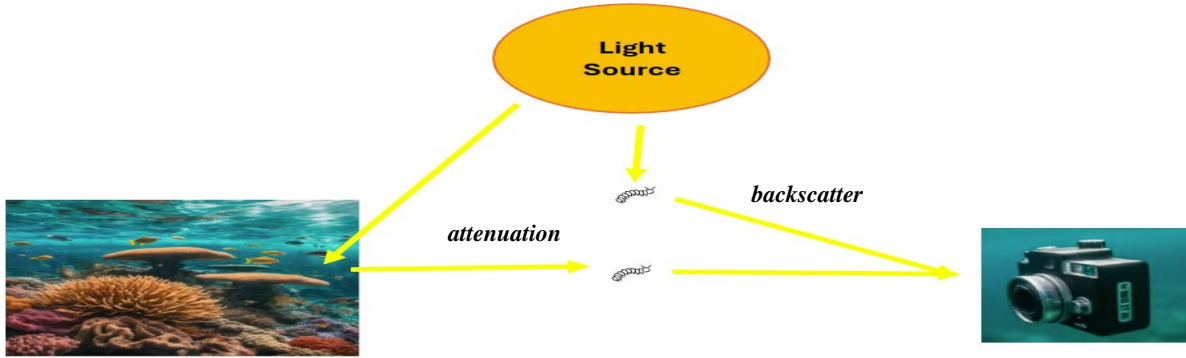


Figure 9. Illustration of the scattering and absorption of light by waterborne particles, which then reflect back to the camera. This phenomenon leads to image degradation by reducing contrast, altering colors, and obscuring fine details, posing significant challenges for underwater imaging and rendering.

Algorithm 1: Estimate Backscatter

- Input:** $I_{sm}, z_{sm}, p_{dark} = 0.01, intervals_num = 25, resized_height = 300$
1. Resize I_{sm} to $resized_height$
 2. Set negative values in I_{sm} to 0
 3. Resize z_{sm} to $resized_height$
 4. Set negative values in z_{sm} to 0
 5. $darkZ, B_c \leftarrow \text{getBackscatterByCurveFittingMultipleImages}(I_{sm}, z_{sm}, p_{dark})$ (i.e., Algorithm 2)
 6. $intervals \leftarrow \text{linspace}(\min(darkZ), \max(darkZ), intervals_num)$
 7. Initialize min_values_depth and $minvals$ as empty lists for each color channel
 8. **for** each color channel k **do**
 - (a) **for** each interval i in $intervals$ **do**
 - i. Find indices ind within the current interval
 - ii. **if** valid data exists **then**
 - A. Append $\min(B_c[ind, k])$ to $minvals[k]$
 - B. Append corresponding $darkZ$ value to $min_values_depth[k]$
 9. Initialize out as a zero matrix
 10. **for** each color channel k **do**
 - (a) Fit model to $min_values_depth[k]$ and $minvals[k]$
 - (b) Extract parameters b_∞ and b_{cb} into out
 11. $B_\infty \leftarrow out[0, :]$
 12. $B_b \leftarrow out[1, :]$
 13. **return** $\{B_\infty, B_b\}$
-

Algorithm 2: Get Backscatter By Curve Fitting Multiple Images

Input: $I, z_{sm}, pdark = 0.01, rho_{flag} = 0, edges_num = 10$

1. Initialize $edges$ with $edges_num$ evenly spaced values between $\min(z_{sm})$ and $\max(z_{sm})$
 2. Compute $zcluster = clusterRange(z_{sm}, edges)$
 3. Initialize $maskRho$ as a zero matrix with the same shape as z_{sm}
 4. **for** i in $range(len(edges) - 1)$ **do**
 - (a) Set $thisMask = (zcluster == i)$
 - (b) **if** $\sum(thisMask) > 0$ **then**
 - i. Extract $thisRho$ using $thisMask$
 - ii. Find darkest pixels in $thisRho$ with threshold $pdark$
 - iii. Update $maskRho$ by adding $thisMaskRho$
 5. Convert $maskRho$ to boolean
 6. Extract darkest pixels and their corresponding depths using $maskRho$ and dm , resulting in $darkZ$ and Bc
 7. **return** $darkZ, Bc$
-

A.5. Experimental Setup

We adopted hyperparameters consistent with those used in [13], as they have shown to yield optimal results empirically. For underwater-specific parameters, we maintained the same learning rates as those used for color. Our data splits involved testing every 8 images, and we utilized the Adam optimizer.

- **Iterations:** 30,000
- **Position Learning Rate Initial:** 0.00016
- **Position Learning Rate Final:** 0.0000016
- **Position Learning Rate Delay Multiplier:** 0.01
- **Position Learning Rate Maximum Steps:** 30,000
- **Feature Learning Rate:** 0.0025
- **Direct Volume Absorption Learning Rate:** 0.0025
- **Backscatter Learning Rate:** 0.0025
- **Opacity Learning Rate:** 0.05
- **Scaling Learning Rate:** 0.005
- **Rotation Learning Rate:** 0.001
- **Lambda SSIM:** 0.3
- **Lambda Backscatter:** 0.1
- **Densification Interval:** 100
- **Opacity Reset Interval:** 3000
- **Densify From Iteration:** 1500
- **Densify Until Iteration:** 15,000
- **Densify Gradient Threshold:** 0.0002
- **Minimum Opacity Threshold:** 0.1

A.6. License Restrictions

Utilizing the [13] code package entails adhering to the following license restrictions:

- **Redistribution:** You may reproduce or distribute the Work only if (a) you do so under this License, (b) include a complete copy of this License with your distribution, and (c) retain all copyright, patent, trademark, or attribution notices present in the Work.
- **Derivative Works:** You may specify additional or different terms for your derivative works of the Work (“Your Terms”) only if (a) Your Terms include the use limitation in Section 2, and (b) you identify the specific derivative works subject to Your Terms. The original License still applies to the Work itself.
- **Other Uses:** Any other use without prior consent of the Licensors is prohibited. Research users must ensure they have all necessary information to use the Software safely.
- **Publications:** If using the Software for a publication, users are encouraged to cite the relevant publications as detailed in the Software documentation.

Additionally, the dataset distribution restrictions from [18] are also enforced.